# Thermal Defect Engineering of Precious Group Metal−Organic Frameworks: A Case Study on Ru/Rh-HKUST-1 Analogues

Werner R. Heinz, Iker Agirrezabal-Telleria, Raphael Junk, Jan Berger, Junjun Wang, Dmitry I. Sharapa, Miryam Gil-Calvo, Ignacio Luz, Mustapha Soukri, Felix Studt, Yuemin Wang, Christof Wöll, Hana Bunzen, Markus Drees, and Roland A. Fischer*

ABSTRACT: A methodology is introduced for controlled postsynthetic thermal defect engineering (TDE) of precious group metal−organic frameworks (PGM MOFs). The case study is based on the Ru/Rh analogues of the archetypical structure $[Cu_3(BTC)_2]$ (HKUST 1; BTC = 1,3,5 benzenetricarboxylate). Quantitative monitoring of the TDE process and extensive characterization of the samples employing a complementary set of analytical and spectroscopic techniques reveal that the compositionally very complex TDE MOF materials result from the elimination and/or fragmentation of ancillary ligands and/or linkers. TDE involves the preferential secession of acetate ligands, intrinsically introduced via coordination modulation during synthesis, and the gradual decarboxylation of ligator sites of the framework linker BTC. Both processes lead to modified Ru/Rh paddlewheel nodes. These nodes exhibit a lowered average oxidation state and more accessible open metal centers, as deduced from surface ligand IR spectroscopy using CO as a probe and supported by density functional theory (DFT) based computations. The monometallic and the mixed metal PGM MOFs systematically differ in their TDE properties and, in particular in the hydride generation ability (HGA). This latter property is an important indicator for the catalytic activity of PGM MOFs, as demonstrated by the ethylene dimerization reaction to 1 butene.

KEYWORDS: metal−organic framework, HKUST 1, Ru BTC, Rh BTC, precious metal, thermal defect engineering, ethylene dimerization, solid−gas interactions
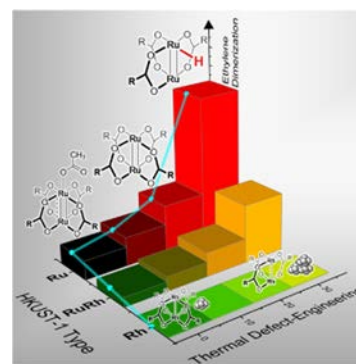
INTRODUCTION

Metal−organic frameworks (MOFs) are unique among solid state materials in structural design and precise molecular tunability[1−3] and, thus, offer fascinating dimensions for potential applications.[4−6] The very high abundance of exposed and accessible reaction centers of defined nature as well as the chemically programmable and confined coordination space of the pore structure render MOFs highly interesting for catalysis.[7−11] Although reticular chemistry naturally strived for perfect compositional definition, highest crystallinity of samples, and thus maximizing framework structural perfection, this paradigm is hence shifting toward also acknowledging the new opportunities that arise from defective structures, a characteristic feature of any solid state material,[12] and thus to compositionally much more complex MOFs.[13−16]

The controlled introduction of defects—termed defect engineering (DE)—has been recognized as a valuable tool of tailoring MOF properties beyond the choice of nodes, linkers, and topology.[17−20] DEMOF design strategies can be grouped into two categories: de novo synthesis, for example, by implementing defect generating (truncated) linkers during synthesis[21−24] and postsynthetic modifications (PSM) of pristine MOFs.[18,25] For example, PSM by thermal annealing (TA) beyond activation is widely used to remove chemisorbed

coordination modulators to yield open metal sites (OMS) at the nodes. UiO 66 has been the prime model case for this concept and as well as HKUST 1 (Cu, Ru) and UHM 3 for exploiting related linker fragmentation processes (e.g., decarboxylation).[13,26−28]

The thermal annealing (TA) could thus become a very attractive and general method for DEMOF synthesis. TA targets the more or less narrow temperature window between activation (desorption of physisorbed guests)[29] and decomposition (collapse of the framework; carbonizing to MOF derived materials).[30−32] However, moving from the more qualitative TA toward a truly quantitative thermal defect engineering (TDE) requires quite a conceptual step ahead in process design and the precise control of thermal PSM of MOFs.

Herein, we want to present our results on TDE of the precious group metal (PGM) based HKUST 1 (Ru, Rh) analogues as the materials of choice for our proof of concept study. The selection is based on the combination of high chemical, thermal, and mechanical stability with defect tolerance and redox flexibility. In addition, our choice is motivated by the importance of PGMs for catalysis on an industrial scale and the lack of fundamental and systematic research on PGM based MOFs. Among the first PGM MOFs to be investigated in some detail were the mixed valent $Ru^{II,III}$ and the univalent $Ru^{II,II}$ analogues of the archetypical $[Cu_3(BTC)_2]$ (HKUST 1; BTC = 1,3,5 benzenedicarboxylate).[33−35] Like the parent structure, the Ru HKUST 1 features tetra connected, dinuclear Ru paddlewheel (PW) nodes. In the mixed valence $Ru^{II,III}$ case, additional chloride (Cl) and acetate (OAc) ligands axially coordinate to the PWs and compensate for the higher oxidation state.[36] The synthesis of Ru HKUST 1 is based on the so called controlled secondary building unit approach (CSA) employing precursors with preformed $M_2(OAc)_2$ PW units. A range of PGM HKUST 1 analogues have been obtained accordingly (M = Ru, Rh[34−40]), including mixed metal congeners with homometallic $Ru^{II,III}$ and $Rh^{II,II}$ nodes in varying molar ratios and doped (Cu, PGM) HKUST 1 derivatives.[41−43] For Ru/Rh HKUST 1, it was found that the preparation of phase pure, crystalline, and highly porous products is strongly reliant on high amounts of acetic acid (HOAc) as the cosolvent.[21,23,44] It acts as a coordination modulator and is retained (chemisorbed) in the final material due to very slow substitution kinetics at the PGM nodes.[18,19] The development of an acetate free synthesis for perfect, i.e., "defect free", compositionally simple PGM HKUST 1 (exactly matching the empirical formula $[M_3(BTC)_2]$) has proved to be highly demanding, and this problem is still not solved.

Herein, we present a comprehensive report on TDE of Ru/Rh HKUST 1 by comparing the univalent $Rh^{II,II}$ and mixed valence $Ru^{II,III}$ with their mixed metal RuRh derivatives together with the univalent $Ru^{II,II}$ based on a complementary set of analytical techniques. We present structure−property relationships on the solid−gas interactions (N_2, CO, H_2, D_2, C_2H_6, C_2H_4) and on the catalytic ethylene dimerization to 1 butene as a test reaction as highlighted in Figure 1.

EXPERIMENTAL SECTION

General Information. Full experimental details regarding utilized reagents, solvents, analytical techniques (instruments), and methods are provided in the Supporting Information (SI). For all prepared samples, an (X/Y) nomenclature will be used, referring to X % Rh feed fraction (incorporation confirmed by inductively coupled plasma mass spectrometry (ICP MS))[40] of the respective parental M MOF (M HKUST 1) and Y % postsynthetically induced defects. Note, the value Y % refers basically to the amount of removed carboxylate ligator sites (CO_2) coordinating to the paddlewheel units of the framework. However, the details are complicated and will be discussed in the main text. An elaborate description of how this empirical parameter was derived based on the analytical data is given in the Supporting Information.

Thermal defect engineering (TDE) was performed using a thermogravimetric analysis (TGA) MS setup operated within an argon filled glovebox. Volatiles were analyzed on line with mass spectrometry (TG MS coupling), and powder X ray diffraction (PXRD) was conducted with Cu Kα radiation in a range of 5−50° 2θ using a Panalytical Empyrean. Analytical C and H contents were determined using a Hekatech EuroEA elemental analyzer, and metal contents (Ru, Rh) were derived from TGA based metal oxide residues (assuming M_2O_3 as confirmed by PXRD) in synthetic air in
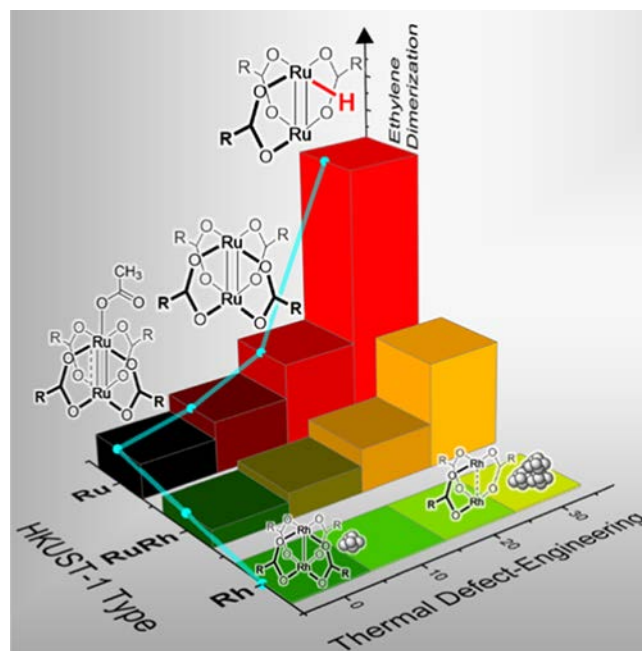

Figure 1. Presented in this work, thermal defect engineering (TDE) of Ru/Rh HKUST 1 activates the materials for efficient ethylene dimerization by creating modified node defects featuring a lower average oxidation state, more accessible metal centers, and M H species as a function of the Ru/Rh composition.

accordance with ICP MS as reported earlier.[40] Repeating units for deriving the empirical formulae were calculated using elemental contents (C, H, M) and a solver based approach using Microsoft Excel (for details, see the SI). Variable temperature PXRD and Fourier transform infrared (FT IR) measurements were conducted with pristine Ru , RuRh , and Rh MOFs (0/0), (50/0), and (100/0). The sorption properties of pristine and defective samples were studied using nitrogen (N_2, 77 K), ethane (C_2H_6), and ethene (C_2H_4), each 278, 288, and 298 K. Density functional theory (DFT) based pore size distributions were determined using N_2 sorption isotherms, and isosteric energies of adsorption for ethane and ethene sorption were determined using Clausius−Clapeyron and Langmuir−Freundlich equations for gas loadings in the range of 10−50 cm^3 g^{-1}. FT IR spectra were recorded from 4000 to 400 cm^{-1} using an attenuated total reflection (ATR) unit, and Raman spectra were recorded from 20 to 2000 cm^{-1} with 532 nm laser wavelength excitation. Variable temperature FT IR was conducted using (0/0), (50/0), (100/0), and $Ru^{II,II}$ samples with N_2, H_2, or D_2 gas flow. High resolution CO probe FT IR spectroscopy was conducted in UHV at low temperatures after treatments at different annealing temperatures for defect creation. All density functional theory (DFT) calculations were performed in ORCA 4.2.0. Minnesota DFT functionals (M06 and M06L) were used with a def2 TZVP basis set and RIJCOSX approximation (see the Supporting information for details).

TDE-MOF Synthesis Method. Pristine samples of Ru MOF (0% Rh), RuRh (50%Rh), and Rh MOF (100%Rh) and a $Ru^{II,II}$ MOF reference sample were prepared in solvothermal reactions following the controlled secondary building unit approach (CSA) as reported earlier.[35,40] After stepwise solvent exchange (H_2O, EtOH, Me_2CO, CH_2Cl_2, each twice), subsequent desolvation (activation in dynamic vacuum at 150 °C, ≈10^{-2} mbar) and basic characterization (PXRD, FT IR, N_2 adsorption), thus obtained pristine, clean MOF samples were further processed using a thermogravimetry instrument (TG) coupled with a mass spectrometer (MS). This led to the definition of thermal defect engineering protocols (TDE) and the reproducible synthesis of samples with defined defectiveness on a preparative microscale (∼30 mg). TDE of the samples was performed using a TG MS setup within a glovebox. This allowed accessibility of both

predefined weight losses and the protection of the obtained highly reactive samples from undesired deactivation in air (e.g., uncontrolled guest sorption or oxidation). TDE MOF sample homogeneity is ensured through a multistep temperature program design (Figure 2)
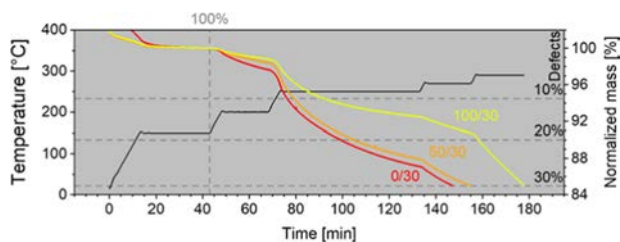

Figure 2. Weight loss profiles and the temperature program for PGM MOF thermal defect engineering (TDE). The plateau at 150 °C between 20 and 40 min (vertical reference line) indicates complete removal of weakly physisorbed species and guests (solvents). The dashed vertical line indicates the point of weight referencing (activated, "clean" sample). The dashed horizontal lines indicate the targeted weight loss for 10, 20, and 30% defectiveness. For experimental details, see the SI.

utilizing successive isothermal steps as a combination of isothermal parts and ramps with constant heating rates.[45] Weight loss monitoring allowed for a controlled TDE between 150 °C (423 K) and 300 °C (573 K) to reproducibly yield samples of specified (Y%) defectiveness. Specifically, predefined analytical mass losses of 5.5, 10, and 15% (due to small molecular mass species $C_xH_yO_z$, e.g., H_2O, CO, CO_2, $H_2C=C=O$) were targeted to yield three series of samples for each pristine MOF of the study. On the basis of elemental analysis and thereof derived sum formulae, different quantitative defect descriptors (%) were calculated depending on the whole organic fraction, removed carboxylate ligator sites (CO_2), and finally including Cl ligands. An overview is provided in Table S3. Using the above mentioned nomenclature, the samples are denoted 10, 20, and 30% defectiveness in the following. However, note that this descriptor is simplified to facilitate sample denomination. Details are discussed in the main text and the SI.

RESULTS AND DISCUSSION

Concept of Study and Leading Questions. Previous work on various kinds of defect engineered and/or hydrogen pretreated Ru HKUST 1[46] revealed a characteristic boost of the catalytic activity in several test reactions such as the Meerwein−Ponndorf−Verley hydride transfer, in the isomer

ization of allylic alcohols to saturated ketones and in selective ethene dimerization to 1 butene.[23,47] These studies raised a number of questions: What is the role of the high amount of residual (chemisorbed) acetate and chloride ligands in the pristine Ru MOF samples and the fate of these species during activation and defect engineering? How are Ru H species formed? How is the metal oxidation state affected during TDE, and how does this correlate with the catalytic activity? To which extent a transfer of findings is possible from Ru to Rh? Can we draw more general conclusions on TDE of MOFs using the above defined model systems as a study case? Previous works on thermal treatments of MOFs typically lack precise analytical monitoring of the process and have mainly been limited to MOF 5 and UiO 66 (and related systems), the investigation of the activation parameters,[29] and removing loosely bound framework components, including coordination modulators.[13,26,48] Our study goes beyond this previous work. It is guided by the idea of targeting controlled linker fragmentation (e.g., decarboxylation) at the temperature window between activation and framework collapse. Since PGM HKUST 1 analogues are thermally very robust and at the same time contain catalytically very versatile and redox active metal centers, we selected them for this detailed case study.

Sample Synthesis: TDE Based on TG-MS Data. Based on the previous report on thermal treatment of Ru HKUST 1,[62] we developed a procedure to reproducibly access different stages of defectiveness in the MOF samples (experimental part, see also the SI). From the TG MS data of the carefully activated samples in the temperature window between 150 and 300 °C, the following information is obtained. For all samples, H_2O, CO, and CO_2 are observed as major elimination species peaking on each temperature increase (Figures S1 and S2). Additional species, in particular ketene ($H_2C=C=O$) and other small $C_xH_yO_z$ fragments (C_3H, $C_2H_4O_2$, $C_2H_2O_3$) are detected. The comparison with literature data on the thermal properties of densely packed (stacked metal sites) metal carboxylates suggests similar decomposition mechanisms taking place in open, highly porous frameworks (isolated metal sites), i.e., MOFs studied herein.[49] In contrast to these species, acetate elimination ($m/z = 60$) takes place at 250 °C almost quantitatively without detectable peaks at lower or higher temperatures. This suggests a preferred removal of

Table 1. Elemental Contents, Calculated Sum Formulae, Derived Metal Charges, and Related N_2 Surface Areas

sample		found C/H/Cl/M_{tot} content (wt %)	ascertained sum formula	mean metal charge	BET surface area ($m^2\ g^{-1}$)	($m^2\ mmol^{-1}$)
Rh-BTC	(100/0)	29.1/1.56/0/41.0	$[Rh_3(BTC)_{1.61}(OAc)_{1.89}]$	+2.24	1360	1025
	(100/10)	28.1/1.30/0/43.1	$[Rh_3(BTC)_{1.22}(IPA)_{0.39}(OAc)_{1.34}]$	+1.92	1340	943
	(100/20)	27.9/1.28/0/45.5	$[Rh_3(BTC)_{0.86}(IPA)_{0.74}(OAc)_{1.01}]$	+1.70	1424	954
	(100/30)	27.6/1.22/0/48.0	$[Rh_3(BTC)_{0.61}(IPA)_{0.99}(OAc)_{0.64}]$	+1.49	1274	812
RuRh-BTC	(50/0)	30.4/1.66/1.5/39.2	$[Ru_{1.44}Rh_{1.56}(BTC)_{1.52}(OAc)_{2.69}Cl_{0.3}]$	+2.53	1211	958
	(50/10)	30.0/1.26/1.5/40.4	$[Ru_{1.44}Rh_{1.56}(BTC)_{1.36}(IPA)_{0.57}(OAc)_{1.03}Cl_{0.3}]$	+2.19	n.d.	n.d.
	(50/20)	28.9/1.26/1.5/42.8	$[Ru_{1.44}Rh_{1.56}(BTC)_{0.64}(IPA)_{1.27}(OAc)_{0.64}Cl_{0.3}]$	+1.80	n.d.	n.d.
	(50/30)	28.3/1.22/1.45/44.8	$[Ru_{1.44}Rh_{1.56}(BTC)_{0.54}(IPA)_{1.27}(OAc)_{0.52}Cl_{0.3}]$	+1.66	n.d.	n.d.
Ru-BTC	(0/0)	29.8/1.34/3.0/37.4	$[Ru_3(BTC)_{1.89}(OAc)_{1.55}Cl_{0.7}]$	+2.64	1018	825
	(0/10)	29.1/1.67/3.0/39.1	$[Ru_3(BTC)_{0.56}(IPA)_{1.32}(OAc)_{1.55}Cl_{0.65}]$	+2.18	1065	801
	(0/20)	30.8/0.93/2.9/41.2	$[Ru_3(BTC)_{0.82}(IPA)_{1.44}(OAc)_0Cl_{0.61}]$	+1.97	1034	755
	(0/30)	28.8/1.04/2.9/43.6	$[Ru_3(BTC)_{1.12}(IPA)_{0.76}(OAc)_{0.24}Cl_{0.57}]$	+1.90	1173	816
	$Ru^{II,II}$	27.4/1.50/0/42.5	$[Ru_3(BTC)_{1.32}(OAc)_{2.22}]$	+2.06	1493	1056

acetate (both monodentate and bridging) over complete BTC elimination or partial BTC ligator site decarboxylation, which takes place mostly at higher temperatures. A differentiation between eliminated monodentate (axial) and bridging (equatorial) acetates is not substantiated on a quantitative basis (for qualitative assignments, CO SLIR and Raman data are discussed below and in Table S2). However, chemical intuition suggests the removal of $OAc_{(axial)} > OAc_{(eq)} > BTC_{(fragmentation)}$ according to hapticity (monodentate vs bridging) and binding properties (with or without framework incorporation/dative or covalent bond). Upon temperature increase to 250 °C, the detection of trace amounts of ^{35}Cl in Ru containing samples indicates the removal of Cl species from the mixed valent $Ru^{II,III}$ nodes. However, as discussed later, elemental analysis revealed the Cl content to be mostly unaffected. Traces of Cl are potentially released in the form of HCl. From a TGA MS experiment with consecutive treatment in N_2 and H_2 atmosphere (Figure S3), we conclude that Cl—although more difficult to be removed in an inert atmosphere (N_2)—readily forms HCl ($m/z = 35$) when TDE is conducted in a H_2 atmosphere and thereby generates M H species (detected by FT IR, vide infra). Upon TDE, the samples darkened, especially the bright green 100% Rh sample. This can indicate the formation of modified PWs and/or of metal nanoparticles. Rh MOF appears to have a slightly higher thermal stability as defect generation requires more time or higher temperatures as compared to Ru MOF.

Composition and Definition of Defectiveness. TGA allows for the quantification of the metal oxide residues (according to ref 40) and, thus, the determination of the total metal content (M_{tot}) of each sample. With the increasing loss of small $C_xH_yO_z$ components (as described above), the "defectiveness" is rising and, consequently, all samples exhibit rising M_{tot} as well (Table 1). This empirical parameter defectiveness can be quantitatively defined in various ways depending on the removed fraction of (a) the nonmetallic content ($C_wH_xO_yCl_z$), (b) the total removed ligands (CH_3CO_2, CO_2, and Cl), or (c) particularly referring to the removed carboxylate ligator sites (CO_2). For reasons of simplicity and to level the slight differences between these different viewpoints, the TDE samples are thus denoted as 10, 20, and 30% defectiveness, respectively. Detailed definitions for defectiveness and related quantitative defect amounts (Table S3) are provided in the SI. The derived M_{tot} were complemented by analytical C, H, and Cl elemental analyses (EA), providing the basis for nonlinear solver assisted empirical sum formulae calculations. As shown previously, C, H, and M contents serve a sufficient basis for a reliable sum formulae calculation utilizing a tailored solver approach.[40] Note that, however, unfortunately, quantitative acid digestion (even in aqua regia) is not possible with these samples. Thus, a reliable quantitative determination of organic components, e.g., BTC, IPA, and OAc proved to be not sufficiently reliable by high performance liquid chromatography (HPLC) or NMR analysis.[40] Defining OAc and BTC as the exclusive organic framework components, the applied solver provides good and reproducible fitting results for the pristine PGM MOFs. For the TDE MOF samples, we nevertheless have to make assumptions for the composition based on the combined analytical and spectroscopic evidence. Thus, the scope of plausible framework components is complemented by isophthalate (IPA) as the decarboxylation product from BTC. Benzoic acid resulting from potential double decarbox

ylation was without regard since BTC is still present in most defective samples. This reasoning is in line with the existing literature.[50,51] Both the experimentally found hydrogen content as well as the derived (formal) mean metal charges correlate well with increasing sample defectiveness defined by TGA, as can be seen in Figure 3. Taking into account that pristine Ru
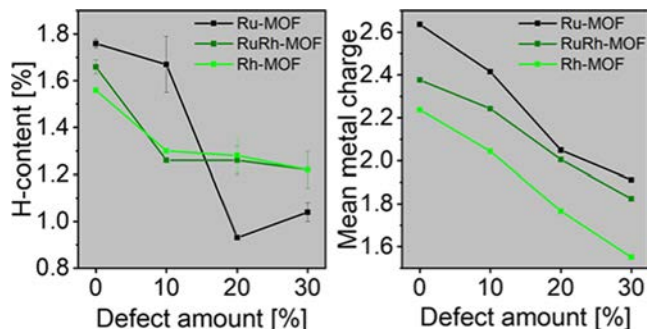

Figure 3. Correlation of the hydrogen content (left) and calculated mean metal charge (right) with sample defectiveness (see definition 1 in the SI). Calculation assuming quantitatively deprotonated carboxylates (OAc, IPA, BTC).

and Rh MOFs should have mean (formal) metal charges of 2.5 and 2.0, the herein obtained values are in good agreement with the expected outcome. A differentiation between axially and equatorially (bridging) bound acetates is shown for pristine MOFs in Table S2. Neither hydrides nor hydroxides nor acidic protons were considered (due to the absence of quantification methods) in the calculation of the formal mean metal charges. Thus, there is some intrinsic uncertainty of the assumed sum formulae. As reported earlier, X ray photoemission spectros copy (XPS) does not allow unambiguous quantification and assignments of metal oxidation states in these PGM MOFs.[40] Alternatives to the herein chosen approach (EA based solver and CO probe FT IR spectroscopy as discussed below) to access metal oxidation states are sophisticated synchrotron techniques like the X ray absorption near edge structure spectroscopy (XANES). Since the high energy X rays particularly required for Ru and Rh are limited to just a few facilities worldwide, such synchrotron based techniques were not available for this study.[40]

All of the obtained TDE MOF samples were then characterized by standard TGA. The resulting graphs are depicted in Figures S10−S12. A correlation between defectiveness and thermal stability can be deduced. The slightly decreasing characteristic decomposition temperatures (above 250 °C) are perfectly aligned with the materials' rising defectiveness. Intuitively, any removal of stabilizing linkers creates an ever more destabilized structure. However, we emphasize that the decrease of thermal stability in DE Cu HKUST 1 (de novo synthesis by defect generating linkers) is much more pronounced with rising defectiveness as compared to TDE PGM HKUST 1 studied herein.[24]

TDE-MOFs: Structure and Stability. Variable temper ature programmed XRD data (VT XRD) of the three pristine Ru/Rh MOF samples 100%Rh, 50%Rh, and 0%Rh are displayed in Figure 4. All three samples preserve their structure until amorphization between 350 and 400 °C, with Ru MOF (0%Rh) showing the highest thermal stability. Amorphization occurs without any intermediate phase transformation for all samples. On first glance, this is inconsistent with TGA based
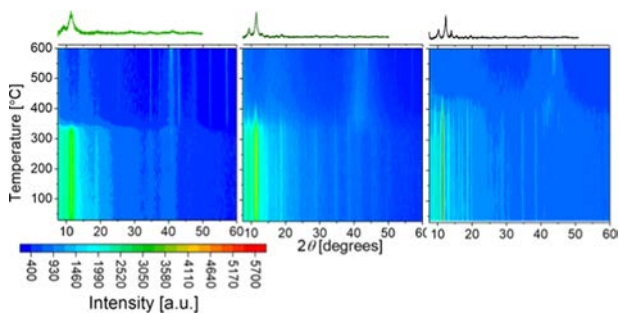
Figure 4. VT XRD pattern contour plots of PGM MOFs. Left: 100% Rh , middle: 50%Rh , and right: 0%Rh sample. Upon higher temperatures, new reflections indicate NP formation. PXRD patterns of pristine MOFs at ambient temperature are shown on top. Note: Additional lines from the Al sample holder become visible.

results, from which Rh BTC seems slightly more stable. As amorphization in general depends on the thermal stability, we primarily attribute these findings to differences in the pristine defect content and crystallite sizes.[52,53] The individual PXRD measurements of all synthesized, still crystalline TDE MOFs indicate retention of the HKUST 1 analogous structure, as can be seen in Figures S4−S6. The 100%Rh sample treated up to 250 °C features broad reflections and, in this case, Rh NP formation ($41.1°$ 2θ) correlates with the defect amount, which is already visible in the (100/10) sample. Additional high resolution transmission electron microscopy (HR TEM) images confirm the formation of metal NPs in Rh containing samples as displayed in Figures S47−S48.

Sorption Properties. *Nitrogen Sorption.* For all samples, nitrogen ad and desorption follows a reversible type I (b) isotherm. Generally, TDE can enhance the gravimetric N_2 surface areas with respect to the pristine MOFs, as shown in Table 1 and Figure 5. The increase in the gravimetric surface area is more pronounced in Ru based materials. Transformed
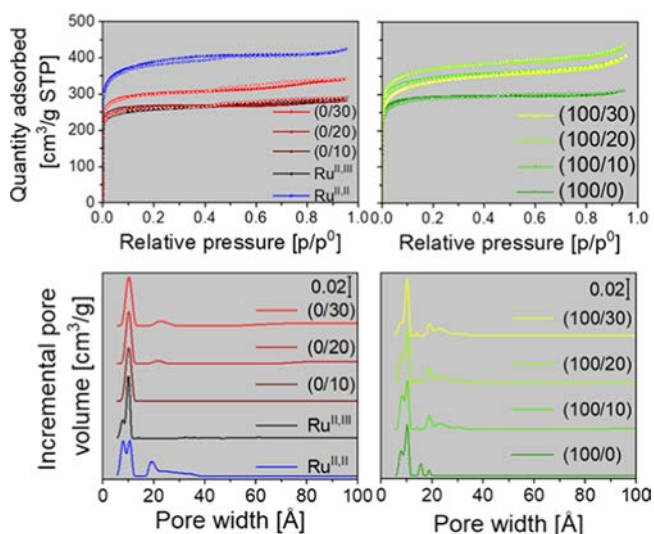

Figure 5. Top: Nitrogen sorption isotherms recorded at 77 K. Closed symbols represent adsorption and open symbols represent desorption branches. Bottom: Incremental pore volumes displaying the DFT derived pore size distribution assuming cylindrical pores on oxide surfaces. Left: 0%Rh series; right: 100%Rh series. TDE leads to an increase in gas uptake and merging of small pores into larger mesopores (see pores > 15 Å).

into molar values, a decrease can be observed, which is attributed to the removal of framework components during TDE and, thus, the lower typical molar mass of the respective repeating units. The still high and preserved porosity is in accordance with predominantly preserved framework struc tures as found through crystallographic and spectroscopic means. All TDE MOFs exhibit a successively reduced number of micropores of ~7−8 Å to the benefit of larger (meso) pores (>15 Å) (see the emerging hysteresis in the plateaus of the TDE isotherms and their PSD plots in Figure 5 and also Figures S17−S20), which is assigned to linker fragmentation via decarboxylation (BTC → IPA) upon TDE. Pristine mixed valence $Ru^{II,III}$ MOF, comprising axial ligands (Cl, OAc), features additional pores. A medium sized micropore of ~9 Å is present. In HKUST 1 type frameworks, three different pores occur: a small one (further called pore A) with ~8 Å and two degenerate pores with ~10 Å size (further called pores B and C). However, the axial positions of the PWs point only into one (pore B) of these degenerate pores. Thus, the presence of axial ligands in mixed valent $Ru^{II,III}$ HKUST 1 causes this pore B to be reduced to ~9 Å, abolishing the degeneration. Upon TDE, axial acetate ligands seem to be removed preferentially as the aforementioned medium sized micropore cannot be observed in TDE Ru MOFs anymore. As reported earlier, the synthesis procedure for the $Ru^{II,II}$ MOF provides a rather defective material also featuring mesopores (see Figure 5).[35]

Ethane and Ethene Sorption. Ethane (C_2H_6) and ethene (C_2H_4) sorption experiments were performed, aiming for correlations with the observed differences of the TDE MOFs in ethene dimerization activity (see below). For ideal, reversible sorption on innocent hosts, adsorbed gas amounts should decrease with higher sorption temperatures. With isotherms recorded at different temperatures (here, 278, 288, and 298 K), the isosteric enthalpy of adsorption (EoA) can be determined. For the saturated hydrocarbon ethane, the trends appear as expected, and (gravimetric) sorption capacities increase with defectiveness (Figures S21−S28, Table S4). In line with the N_2 based results, the sample (100/20) has the highest ethane uptake within the Rh series. Within the Ru series, the uptake also increases with defectiveness and the $Ru^{II,II}$ sample allows the highest uptake. The desorption of ethane is quantitative for all samples, suggesting fully reversible sorption processes. The derived EoAs for ethane can be seen in Figure 6. Ru based TDE MOFs have only subtle differences in ethane sorption enthalpies, which decrease with higher loadings (left graph), suggesting preferred adsorption sites as also observed for Cu HKSUT 1.[54] Interestingly, the univalent Ru MOF features lower EoA (≈ 25 kJ mol^{-1}) than the mixed valent Ru MOF (≈ 30 kJ mol^{-1}). Temperature induced removal of axially bound OAc seems to render the pore environment less lipophilic. In contrast, on Rh samples, ethane EoAs are independent of the loading but generally increase upon TDE from ≈ 30 kJ mol^{-1} in pristine Rh MOF up to ≈ 40 kJ mol^{-1} in the (100/20) sample (right graph).

The ethene (C_2H_4) sorption isotherms are depicted in Figures S29 and S30. Strong hysteresis between adsorption and desorption branches as well as significant amounts of irreversibly adsorbed species (further called residues) are observed most predominantly for TDE MOFs. Such behavior of inversed temperature trends to what was anticipated has been rarely reported in the MOF literature so far.[55,56] These other data were assigned to pore window blocking at low temperatures. Herein, however, we assign our data to a partial
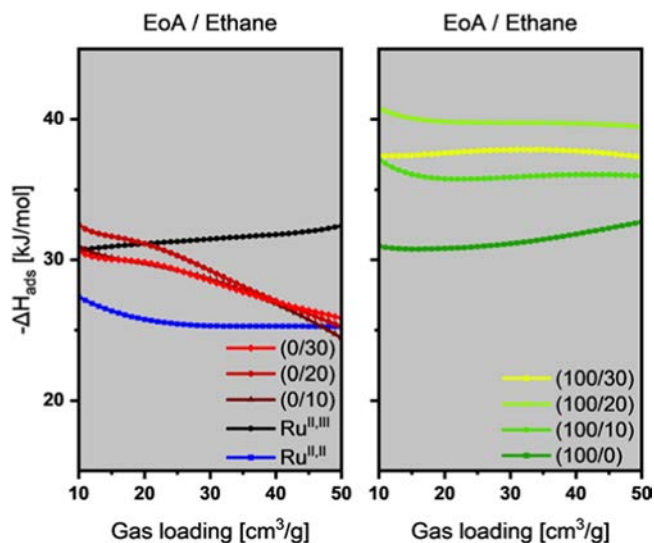
Figure 6. Isosteric enthalpy of adsorption for ethane derived from sorption isotherms. Left: Ru based MOFs; right: Rh based MOFs. No energetic differences can be observed for TDE MOFs. Energies of adsorption slightly decrease upon higher loadings. For Rh TDE MOFs, EoA increases upon TDE peaking in (100/20).

chemisorption of ethene (e.g., to some chemical reactivity at the nodes). This correlates with temperature dependence and counteracts the anticipated physisorption behavior inverting the expected trend. Unfortunately, this effect prevents meaningful EoA calculations for comparison. Nevertheless, some additional conclusions can be drawn from ethene sorption isotherms. Based on the molar uptake and amounts of residues (mmol g_{MOF}^{-1}), we estimated the number of adsorbed ethene molecules per paddlewheel unit. Correlation of ethene uptakes and residues with sorption temperature and sample defectiveness was visualized in contour plots displayed in Figure 7. Strong chemisorption of ethene occurs on Ru MOF and on Rh MOF (most certainly at OMS: see Figures S21 and S22 for N_2 isotherms and PSDs after repeated ethene sorption according to literature reports[57,58]). However, some additional reactivity seems to be exclusive for Ru based MOFs. This can be concluded from the significantly increased amounts of residues at the highest sorption temperature (see Tables S5 and S6). Drastically increased uptake and residues for the most defective (0/30) Ru MOF sample suggest the highest reactivity toward ethene in this series. In line with the postulated TDE induced metal reduction to Ru$^{\delta+}$ species (see below), the Ru^{II,II} reference sample (see the band on top of the Ru residue contour map in Figure 7) perfectly follows the same temperature dependence. This is in line with the hydride generating ability (HGA) of Ru MOF discussed later (see IR spectra in Figure 8, bottom left graph) being a prerequisite for ethene dimerization (or oligomerization) reactivity.

To summarize sorption properties, TDE does not critically affect the porous structure of the pristine MOFs, but partial linker fragmentation (decarboxylation BTC $\rightarrow$ IPA + CO_2) and/or removal (OAc $\rightarrow$ $CO/CO_2/C_xH_yO_z$) supports a mesopore formation in all materials. For ethane, enthalpy of adsorption is ≈30 kJ mol^{-1} for Ru MOFs irrespective of their defectiveness, while defects in Rh MOFs clearly increase EoAs up to ≈40 kJ mol^{-1}. Typical for nonreactive sorbents, lower sorption temperatures allow higher gas uptakes for ethane.
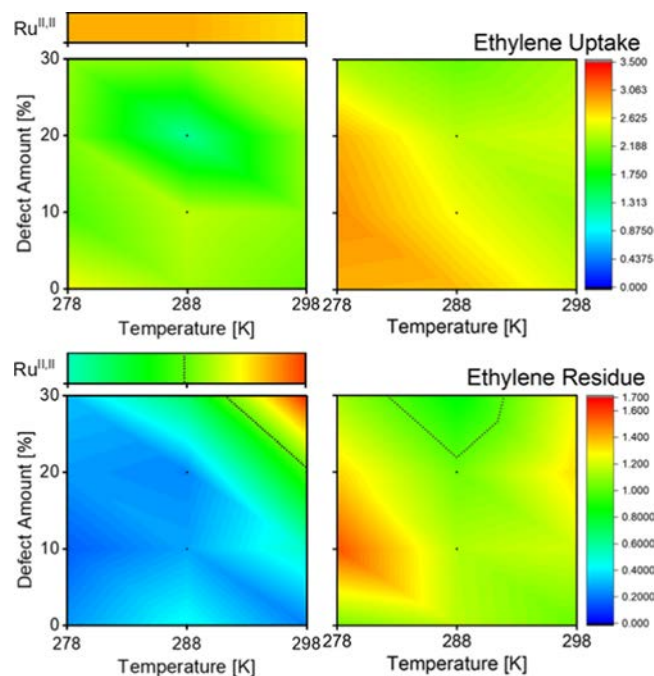

Figure 7. Contour plots of ethylene sorption: Left side: Ru ; right side: Rh MOFs. Top row: uptake in molecules per PW. Bottom row: residue in molecules per PW. The dashed isoline represents the threshold of one molecule per PW. A different visualization is shown in Figures S31 and S32.

There is strong ethene uptake for Ru MOF and Rh MOF, rather irrespective of both the temperature and defectiveness peaking at the Ru^{II,II} sample. Both metals obviously bind ethene strongly. Thus, ethene residues remain bound in the materials after desorption. In Rh MOFs, roughly one molecule of ethene per PW remains bound, rather independent of sorption temperature and sample defectiveness. Opposingly, defective Ru MOFs and particularly their univalent Ru^{II,II} analogue trap increasing amounts of ethene at higher temperatures, indicating a reactive sorption (chemisorption). Residues exceeding one molecule ethene bound per PW support the postulated reduction and generation of more OMS upon TDE.

Vibrational Spectroscopy. To gain comprehensive insights into the bonding situation, both FT IR and Raman spectros copy were applied (including CO as a probe molecule) and further supported by computational calculations on model molecules allowing assignment of individual vibration modes (see Table S7).

Almost identical FT IR spectra support the overall isostructurality of all samples as shown in Figure 8 (top graph) and Figures S33−S35. Significant changes, however, occur upon TDE, particularly with Ru MOF (0%Rh samples). Generally, in carboxylate based coordination compounds, the valence modes of COO are very sensitive toward changes at the metal center due to their direct bonds and close vicinities.[59] Here, a hypochromic shift of $\nu_{as}(COO)$ of mixed valent Ru^{II,III} MOF results in a band shape and position identical to the univalent 100%Rh and the Ru^{II,II} reference sample as displayed in the bottom right graph in Figure 8. This is explained by the hypothesis of a thermally induced metal reduction of the mixed valence Ru^{II,III} to the univalent Ru^{II,II}, as a consequence of axial ligand removal. As the chloride content of the Ru containing samples does not change significantly,
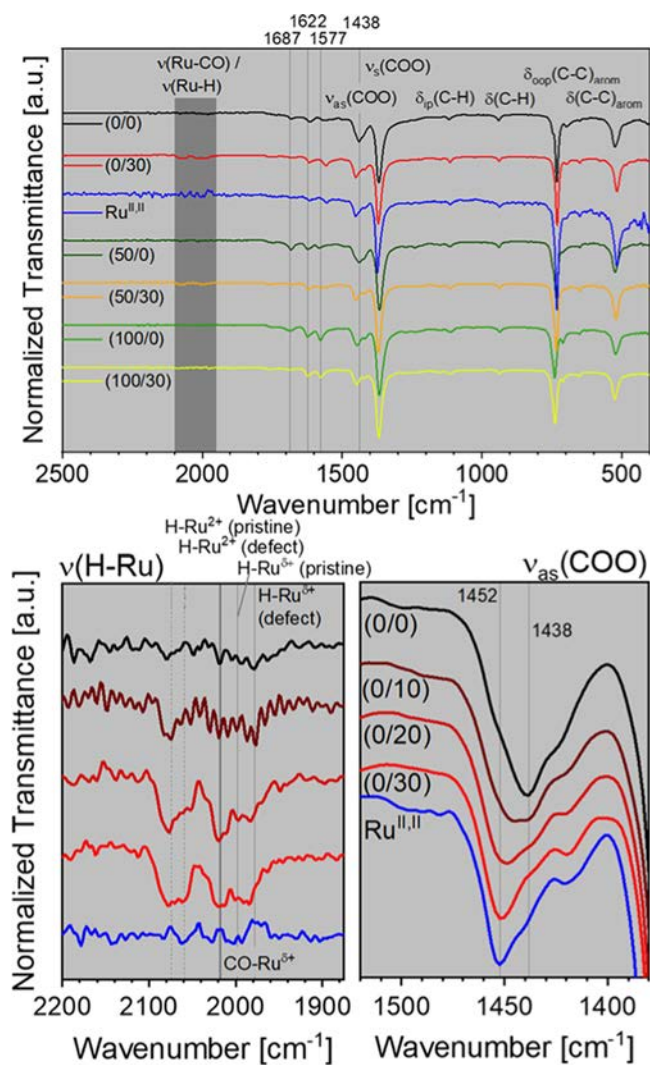
Figure 8. Top: FT IR spectra of selected TDE MOF and Ru^{II,II} samples revealing the general bonding similarity. Bottom: zoom ins of highlighted regions for Ru MOF samples. Left: emerging Ru H (dashed lines: Ru^{2+} H, compact lines: Ru$^{\delta+}$ H and Ru CO (bold line) bands upon TDE). Intensities are scaled by a factor of 3. Right: blue shift of ν_{as}(COO) suggests axial acetate removal and reduction toward Ru^{II,II} nodes upon TDE.

axial acetate must be preferentially removed. This is in accordance with the existing literature on isolated dimeric Ru tetra and pentacarboxylate complexes.[60,61] Low intensity signals resulting from weakly bound carboxylates ($\approx$1687 cm^{-1}) mainly occur in the (50/0) and (100/0) samples and disappear upon TDE.[62−65]

In line with the FT IR spectra of the whole series, recorded Raman spectra support the removal of axial ligands and decarboxylation (see Figures S36−S38 and Table S7). The spectra coincide with most of the signals throughout the series of samples. Nevertheless, three characteristic effects can be observed: (1) Vibration modes attributed to axial ligands present in Ru containing samples mainly disappear in the course of TDE. The ν(Ru Cl) bands at 276 cm^{-1} exhibit only slightly decreased intensity, while ν(Ru OAc$_{axial}$) at 324 cm^{-1} almost completely disappears. (2) Weakly bound or free carboxylates are readily removed by TDE from 100% Rh sample, as indicated by the disappearing signal at 1688 cm^{-1}. The broadening of the band attributed to ν_s(C=C)$_{arom}$ (at

1606 cm^{-1}) suggests a modification of the aromatic scaffold, which might be caused by the assumed linker decarboxylation, thus representing the increasing abundance of IPA with respect to the parent BTC linker. This supports the validity of the applied solver approach, including IPA, as a potential framework constituent.

Hydride Generating Ability (HGA). Upon TDE, H Ru (hydride) species can be identified according to the emerging bands ranging from 2100 to 1950 cm^{-1}.[66] As indicated in the bottom left graph in Figure 8, H Ru^{2+} (dashed lines at 2074 and 2059 cm^{-1}) emerge at an early stage of defect formation (samples (0/10) and (0/20)), while reduced site H Ru$^{\delta+}$ preferentially emerge in highly defective samples. The signal assignment is based on literature information.[23,47] The observation of hydrides is remarkable since TDE is performed in an inert atmosphere without any supply of H$_2$ gas. However, in line with the literature, an alternative thermal treatment at 150 °C in a H$_2$ atmosphere yields identical Ru H species. As demonstrated previously, the formation of these metal hydrides appears to be a key requisite for ethene dimerization reactivity and can enhance hydride transfer reactions.[46,47,67] It remains unclear at this level of our study how the mechanism for metal hydride formation proceeds under otherwise inert conditions. We assume the decomposition of hydrogen containing framework components (OAc, BTC) by radical mechanisms and/or by concerted C−H activation and potential H transfer to the metal nodes. Interestingly, such species are barely visible in Rh based TDE MOFs, revealing significant differences in the metal based HGA (see Figures S33−S35). This is supported by very weak rhodium hydride signals even after H$_2$ or D$_2$ treatment (see Figures S39 and S40) and a neglectable ethene dimerization activity, as will be discussed later.

To gain deeper insights into the differences of the applied materials, we utilized more elaborate IR studies using variable temperatures and CO probing at low temperatures under UHV conditions, which are part of the discussion in the next chapter.

CO Probe FT-IR Spectroscopy. The controlled introduction of defects in the MOFs via TDE was monitored by the CO SLIR (surface ligand IR spectroscopy) approach,[68] highly sensitive to the oxidation states and coordination environments of metal atoms. Figure 9 shows the corresponding IR results for different TDE MOFs after exposure to CO recorded at 105 K. Clearly, a number of distinctly different bands are observed. On the basis of previous work[21] and the present new findings, these characteristic bands are assigned in Table 2.

The mixed valent, pristine (activated) Ru MOF is dominated by two characteristic CO bands at 2171 cm^{-1} (OC Ru^{3+}) and 2135 cm^{-1} (OC Ru^{2+}), which have been reported previously.[21] The TDE of Ru MOF at elevated temperatures leads to the appearance of two new low frequency peaks at 2040 and 1996 cm^{-1}, which are assigned to OC Ru$^{\delta+}$ species (CO bound to reduced electron rich Ru centers) with lower Ru coordination numbers. This conclusion is in line with the observation of similar frequencies reported for Ru OMS of DE Ru HKUST 1 prepared by the mixed linker approach.[22,23,44] The formation of Ru$^{\delta+}$ defects in TDE Ru MOF samples is further accompanied by a slight red shift of the OC Ru^{2+} bands from 2135 to 2122 cm^{-1}. This feature is assigned to the structural and electronic modifications of Ru dimer nodes caused by thermal decarboxylation.

This is in line with the spectrum of the univalent Ru^{II,II} sample, which already in its pristine state seems to be
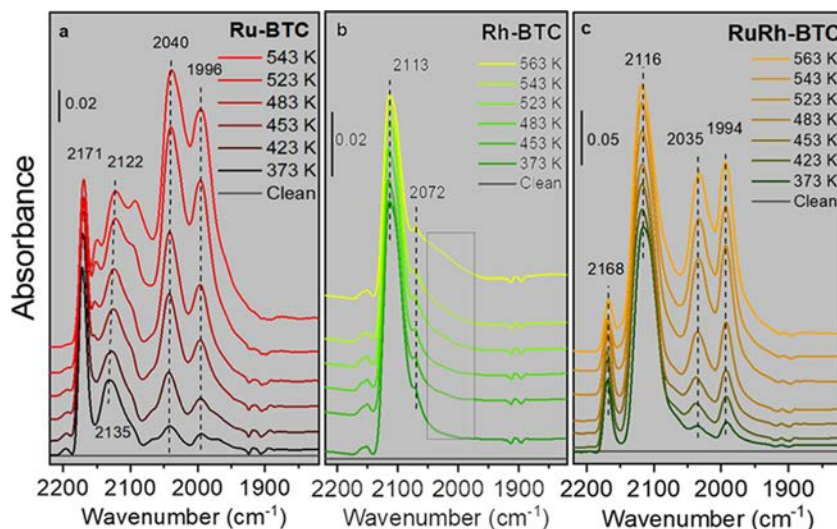
Figure 9. UHV FTIRS data obtained after CO adsorption (0.01 mbar) on different pristine and TDE PGM MOFs at 105 K. Before CO adsorption, the samples were preheated at the indicated temperatures (373−563 K) for in situ defect generation: (a) Ru MOF (0% Rh); (b) Rh MOF (100% Rh); and (c) Ru/Rh MOF (50% Rh).

Table 2. CO FT IR Probe Spectroscopy[a]

sample	band (cm⁻¹)	assignment
Ru-MOF	2171	Ru^{3+}-CO
	2135 2122	Ru^{2+}-CO
	2040, 1996	$Ru^{\delta+}$-CO
Rh-MOF	2113	Rh^{2+}-CO
	2072	Rh^{1+}-CO
RuRh-MOF	2168	Ru^{3+}-CO
	2116	Rh^{2+}-CO
	2035,1994	$Ru^{\delta+}$-CO
Cu-HKUST-1[27]	2179	Cu^{2+}-CO
	2156[b]	Cu^{+}-$(CO)_2$
	2121	Cu^{+}-CO
UHM-3[28]	2175	Cu^{2+}-CO
	2153	unclear[c]
	2118	Cu^{+}-CO

[a]Assignment of bands for PGM MOF samples, including Cu HKUST 1 and UHM 3 literature values. [b]Putative assignment. [c]We assume $Cu^{+}(CO)_2$ similar to the Literature.[27]

dominated by a related and rather defective structure (see sorption data in Figures 5 and S46). As shown in Figure 9a, the defect related CO bands gain substantial intensity only after annealing the sample to temperatures at or higher than 480 K. The situation is thus similar to Cu based UHM 3[28] and HKUST 1.[27,69] However, in these different MOFs, TDE was found to occur at lower temperatures (370−420 K). Thus, Ru[II,III] HKUST 1 reveals a higher thermal stability as compared to the Cu PW based analogues.[27,28] The CO SLIR data for the pristine Rh HKUST 1 exhibits one intense IR band at 2113 cm⁻¹ (Figure 9b), which is attributed to an OC Rh[2+] species. We assign the weak shoulder at 2072 cm⁻¹ to a small amount of reduced OC Rh[1+] defect sites. The spectral evolution along with the annealing to higher temperatures reveals that the Rh[II,II] MOF is slightly more stable (a significant decrease of the OC Rh[2+] band occurs at T > 540 K) than the Ru[II,III] MOF, which is in excellent agreement with the TGA based data (see Figures 2 and S9−S11). Furthermore, the IR signal at 2153 cm⁻¹ indicates the presence

of a geminal dicarbonyl species $(OC)_2Rh^{1+}$, indicating a reduced Rh[1+] site being 2 fold coordinatively unsaturated.[24]

Upon further heating and annealing above 560 K, a broad feature appears at about 2000−2060 cm⁻¹. Such low vibrational frequencies suggest the presence of (uncharged) metal Rh nanoparticles, resulting from a progressive thermal decomposition of the MOF framework. This is in line with PXRD data (Figures S4−S9).

The pristine RuRh MOF (50%Rh) is characterized by two dominating IR bands at 2168 and 2116 cm⁻¹ originating from OC Ru[3+] and OC Rh[2+] species, respectively (Figure 9c). As observed and discussed earlier, the mixed metal sample presumably comprises a statistic mixture of monometallic PWs rather than mixed metal PWs.[40] The band assignment is further supported by temperature dependent CO SLIR. As shown in Figure S45, CO desorbs from Ru[3+] sites already at about 130 K, while for Rh[2+] and Rh[1+] sites, substantially higher desorption temperatures (above 320 K) are observed. We explain this by stronger bonds, resulting from additional charge available for π backdonation in relation to OC Ru[3+], as confirmed by DFT calculations (see Table 3). For the TDE

Table 3. Computed binding energies (E_{ads}) and vibrational frequencies (ν_{CO}) of CO adsorbed on Rh PWs

system	E_{ads} (kJ mol⁻¹)	ν_{CO} (cm⁻¹)[a] (shift from gas CO)
Gas CO		2143
Pristine-CO	97	2096 (47)
Pristine-2CO	63	2097 (46)
Defect-CO	224	2044 (99)
Defect-2CO	203	2065 (78)

[a]Scaled with respect to gas CO.

MOFs heated to elevated temperatures (c), we clearly see two additional vibrations at 2035 and 1994 cm⁻¹, demonstrating the creation of reduced Ru[δ+] defects. These peaks dominate only after heating to T > 520 K, revealing a higher thermal stability of bimetallic RuRh MOFs relative to the monometallic Ru[II,III] analogue.

We have further carried out DFT calculations to gain deeper insights into the interaction of CO with pristine and TDE Rh MOFs. Figure 10 shows the DFT optimized atomic structures
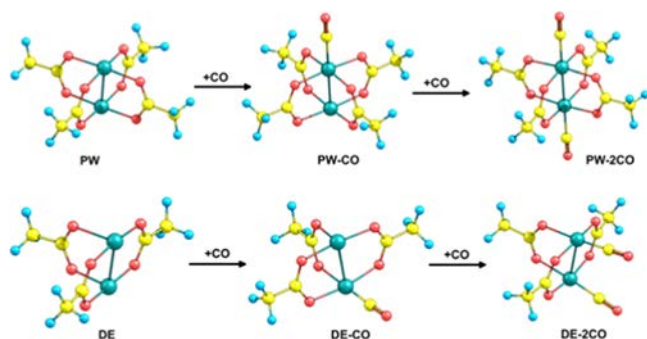

Figure 10. DFT optimized atomic structures of CO adsorption on pristine and defect engineered Rh PWs. Carbon, yellow; oxygen, pink; hydrogen, blue; and rhodium, turquoise.

of various CO species bound to intact Rh^{2+}/Rh^{2+} as well as reduced Rh^+/Rh^{2+} dimers. The corresponding CO stretching frequencies and binding energies are summarized in Table 3 (see the SI, Tables S8 and S19 and Figures S49−S59 for details). Overall, there is good agreement between the computed and experimental results (see Table 2). We note that in the case of reduced Rh^+/Rh^{2+} paddlewheels, the adsorption of two CO molecules (one CO at each of the two Rh cations) leads to a blue shift in frequency (21 cm^{-1}) compared to that of the one CO structure (Figure 10). This is attributed to the electronic redistribution of the reduced Rh dimers along with the second CO adsorption. Furthermore, computations reveal that the adsorption of CO on Rh^+/Rh^{2+} defects can stabilize the low spin state of the system. Accordingly, CO binds stronger to Rh^+/Rh^{2+} than to pristine paddlewheels (Table 3), in line with the temperature dependent IR observation (Figures S41−S45). In addition, CO sorption experiments were conducted at higher temperatures and at ambient pressure (see desorption graphs in Figure 11). The binding of CO at OMS was examined after
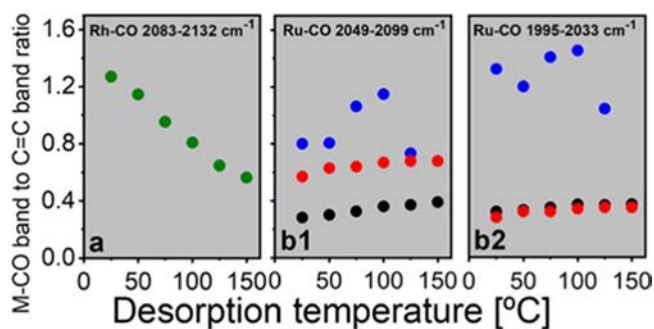

Figure 11. Ratio of the integrated band areas for Rh CO (a) and the two bands for Ru CO (b1, b2) to $\nu(C=C)_{arom}$ as a function of desorption temperature in N$_2$. MOF catalysts were pretreated at 150 °C in N$_2$ and CO adsorbed at 30 °C. The mixed valent Ru BTC is indicated with black (150 °C N$_2$ pretreatment) and red (300 °C N$_2$ pretreatment simulating the (0/30) sample), and univalent $Ru^{II,II}$ with blue data points. The data indicates labile CO binding to Rh but strong interactions with Ru sites and increasing OMS. The increase in b1 (red data points) suggests a preferred removal of axial over equatorial acetate.

CO adsorption at room temperature and its controlled desorption up to 150 °C. Thus, Figure 11 shows the ratios of the integrated band areas for Rh (a: 2083−2132 cm^{-1}) and for Ru (b1: 2049−2099 cm^{-1} and b2: 1995−2033 cm^{-1}) as a function of the area of the samples' C=C band (∼1390 cm^{-1}). All individual FT IR spectra are provided in the SI (Figures S41−S44). The strong binding of CO onto Ru sites, either in $Ru^{II,III}$ or $Ru^{II,II}$, as compared to Rh sites, becomes evident with the slope for increasing desorption temperatures.

Compared to the pristine Ru MOF (treated at 150 °C, 10 min, black data points), a short pretreatment at 300 °C (10 min, red data points) roughly doubles the intensity of CO band b1, which is in accordance with the observation that the number of OMS also roughly doubles (see TGA based CO titration experiment displayed in Figures S13−S16 and Table S1). Interestingly, the CO band b2, which can be assigned to partially reduced, defective $Ru^{\delta+}$ sites, does not increase with the (short time) thermal treatment of mixed valent Ru MOF but merely shows a strong increase for the univalent $Ru^{II,II}$ sample. With respect to the band assignments discussed before, we conclude a preferred removal of axial over equatorial (bridging) acetates first, giving more Ru^{2+} sites prior to the formation of defective $Ru^{\delta+}$ sites. Thus, we assume the aforementioned order of ligand removal/fragmentation $OAc_{(axial)} > OAc_{(eq)} > BTC_{(fragmentation)}$, which is also consistent with the trends observed for $\nu_{as}(COO)$ as highlighted in Figure 8 (IR, bottom right graph). The different material properties with respect to metal, oxidation state, and their manipulation using the controlled TDE render these materials interesting for catalysis, as detailed below.

Catalytic Ethene Dimerization. As outlined in the previous subchapter, the HGA in the TDE MOFs and their relevance in catalysis was placed under scrutiny using ethene dimerization to 1 butene as a probe reaction. The samples were thermally treated in N$_2$ for defect generation and in situ metal hydride formation prior to ethene dimerization. Ru based MOF samples were treated at 300 °C (N$_2$), and intrinsic Ru H formation takes place at this condition; however, the HGA at Rh sites required additional treatment under hydrogen. We used D$_2$ for unambiguous detection of such hydride formation and indeed observed a second band assigned to Rh D. Figure 12 shows ethene dimerization turnover frequencies (TOF, per total metal, M_{tot}) as a function of the Ru content in the TDE
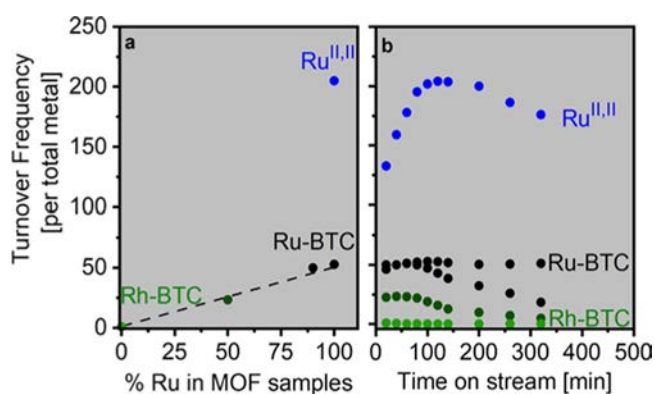

Figure 12. (a) Ethene dimerization turnover frequency (TOF) per total metal per hour as a function of the Ru content at 5 bar and 50 °C; (b) TOF as a function of time on stream. Besides Rh BTC, Ru BTC, $Ru^{II,II}$ BTC, and the 50% Rh sample, a RuRh (90:10) BTC sample (10% Rh) was investigated.

MOF samples at 50 °C and 5 bar ethene. Such conditions enable a correct catalyst comparison under gaseous conditions and avoid different solvation phenomena in catalysis via intrapore condensation.[47] As observed in the linear trend of TOF values, the 100%Rh MOF shows much less activity for C−C coupling reactions into ethene dimers even after the additional hydride formation with H_2/D_2. This is despite the more accessible univalent Rh nodes as a consequence of the absence of axial chloride or acetates compared to the mixed valent Ru nodes. With the increasing Ru content, the PGM MOFs are much more catalytically active. This is in accordance with the trends seen in the hydride generating ability (HGA) upon TDE.

Such differences between Ru MOF and Rh MOF also become evident when the Ru oxidations states are modified by TDE. After thermal treatment at 300 °C in N_2, the TDE $Ru^{II,II}$ MOF catalyst shows about four times higher activity in ethene dimerization than the mixed valent pristine $Ru^{II,III}$ MOF and is thus superior to the previously reported Ru based MOF catalysts under the same reaction conditions.[47] These results confirm the relevance of the metal choice, its hydride generating ability (HGA) upon TDE, and the oxidation state. TDE yields lower average Ru oxidation states if starting out with the univalent $Ru^{II,II}$ MOF as compared to the mixed valence $Ru^{II,III}$ MOF. In addition, the TOF values as a function of time on stream (Figure 12b) show a pronounced induction period for $Ru^{II,II}$, in contact with ethylene at 5 bar (which has been reported for Ru MOF earlier[47]). This can be attributed to the enhanced HGA in the ethene stream even at 50 °C. Once at maximum TOF values, however, the activity for $Ru^{II,II}$ shows a steady decay, attributed to the progressive deposition of larger oligomers. However, since all MOF catalysts show a 100% selectivity to 1 butene (within the detection limits), these oligomers must be formed in trace amounts. As reported earlier,[47] higher ethene pressures leading to intrapore solvation phenomena can inhibit these oligomers and, thus, should avoid such a progressive deactivation. A comparison between the catalytic performance of this and previous works is provided in Table S20.

CONCLUSIONS

In summary, the present study demonstrates a methodology for postsynthetic thermal defect engineering (TDE) used to systematically access well defined precious group metal (PGM) TDE MOFs (Ru/Rh HKUST 1 analogues). Characterization with a complementary set of analytical techniques (VT PXRD, FT IR, Raman, HR TEM, TGA, EA, N_2, C_2H_6, and C_2H_4 physisorption and CO probe FT IR spectroscopy in UHV) shows that these compositionally very complex materials undergo a successive reduction of the PGM centers at the dimeric metal nodes by ligand/linker removal or fragmentation upon TDE (a set of the putative defective (modified) PW structures is provided in Schemes S1 and S2). This can occur via complete removal of modulator based acetate ligands or through decarboxylation of framework linkers (BTC → IPA). Both processes generate more open and partially reduced metal sites; thus, the average oxidation state of the PGM paddlewheel nodes is lowered as seen by CO SLIR analysis and related DFT based computations. In the mixed valent $Ru^{II,III}$ HKUST 1 case, the additional axial acetate or chloride ligand accounting for the higher charge strongly impacts the occurring reduction process. While axial acetates are readily removed, the reduction of metal nodes comprising

chloride counterions requires harsher conditions. A remarkable hydride generating ability (HGA) and redox flexibility during TDE are observed for Ru MOFs, while with increasing Rh content reduction toward Rh^0 (nanoparticle formation) becomes relevant.

Investigation of the catalytic ethene dimerization as the test reaction peaked in a four fold activity increase of TDE $Ru^{II,II}$ HKUST 1 compared to the best result previously reported for TDE $Ru^{II,III}$ HKUST 1 as schematically displayed in Figure 1.[47]

From our data, we deduce the suggestion to take advantage of the comparably high kinetic and, in particular thermal stability of PGM MOFs. We highlight careful in situ monitored thermal defect engineering as a tool to tailor the defect structure quantitatively and reproducibly and thus to modulate the catalytic properties of the materials. There should be much room for design and tailoring PGM MOFs and their TDE derivatives much beyond the scope of this conceptual study.

AUTHOR INFORMATION

Corresponding Author

Roland A. Fischer − *Department of Chemistry, Chair of Inorganic and Metal Organic Chemistry, Technical University of Munich (TUM), 85748 Garching, Germany;* orcid.org/0000 0002 7532 5286; Email: roland.fischer@tum.de

Authors

Werner R. Heinz − *Department of Chemistry, Chair of Inorganic and Metal Organic Chemistry, Technical University of Munich (TUM), 85748 Garching, Germany*

Iker Agirrezabal Telleria − *Department of Chemical and Environmental Engineering, Engineering School of the University of the Basque Country (UPV/EHU), 48013 Bilbao, Spain*

Raphael Junk − *Department of Chemistry, Chair of Inorganic and Metal Organic Chemistry, Technical University of Munich (TUM), 85748 Garching, Germany*

Jan Berger − *Department of Chemistry, Chair of Inorganic and Metal Organic Chemistry, Technical University of Munich (TUM), 85748 Garching, Germany;* orcid.org/0000 0002 9230 0398

Junjun Wang − *Institute of Functional Interfaces (IFG), Karlsruhe Institute of Technology (KIT), 76344 Eggenstein Leopoldshafen, Germany*

Dmitry I. Sharapa − *Institute of Catalysis Research and Technology (IKFT), Karlsruhe Institute of Technology (KIT), 76344 Eggenstein Leopoldshafen, Germany;* orcid.org/0000 0001 9510 9081

Miryam Gil Calvo − *Department of Chemical and Environmental Engineering, Engineering School of the University of the Basque Country (UPV/EHU), 48013 Bilbao, Spain*

Ignacio Luz − *RTI International, Durham, North Carolina 27709, United States;* orcid.org/0000 0002 5020 9211

Mustapha Soukri − *RTI International, Durham, North Carolina 27709, United States;* orcid.org/0000 0002 8512 8067

Felix Studt − *Institute of Catalysis Research and Technology (IKFT), Karlsruhe Institute of Technology (KIT), 76344 Eggenstein Leopoldshafen, Germany;* orcid.org/0000 0001 6841 4232

Yuemin Wang − *Institute of Functional Interfaces (IFG), Karlsruhe Institute of Technology (KIT), 76344 Eggenstein Leopoldshafen, Germany;* orcid.org/0000 0002 9963 5473

Christof Wöll − *Institute of Functional Interfaces (IFG), Karlsruhe Institute of Technology (KIT), 76344 Eggenstein Leopoldshafen, Germany;* orcid.org/0000 0003 1078 3304

Hana Bunzen − *Chair of Solid State and Materials Chemistry, Institute of Physics, University of Augsburg, 86159 Augsburg, Germany*

Markus Drees − *Department of Chemistry, Chair of Inorganic and Metal Organic Chemistry, Technical University of Munich (TUM), 85748 Garching, Germany*

Author Contributions

This manuscript was written through contributions of all authors.

ABBREVIATIONS

BDC, benzene dicarboxylate
BET, Brunauer−Emmett−Teller
BTC, benzene tricarboxylate
CSA, controlled secondary building unit approach
DE, defect engineering
DFT, density functional theory
EA, elemental analysis
EDX, energy dispersive X ray spectroscopy
EoA, enthalpy of adsorption
SI, supporting information
FT IR, Fourier transform infrared (spectroscopy)
HGA, hydride generating ability
HKUST, Hong Kong University of Science and Technology
MOF, metal−organic framework
MS, mass spectrometry
NP, nanoparticle
PSD, pore size distribution
PW, paddlewheel
PXRD, powder X ray diffraction

SLIR, surface ligand IR spectroscopy
TA, thermal annealing
TDE, thermal defect engineering
TGA, thermogravimetric analysis
TOF, turnover frequency
UHV, ultrahigh vacuum
VT, variable temperature

REFERENCES

(1) Zhou, H. C.; Long, J. R.; Yaghi, O. M. Introduction to Metal−Organic Frameworks. *Chem. Rev.* **2012**, *112*, 673−674.

(2) Zhou, H. C. J.; Kitagawa, S. Metal−Organic Frameworks (MOFs). *Chem. Soc. Rev.* **2014**, *43*, 5415−5418.

(3) Yaghi, O. M.; O'Keeffe, M.; Ockwig, N. W.; Chae, H. K.; Eddaoudi, M.; Kim, J. Reticular Synthesis and the Design of New Materials. *Nature* **2003**, *423*, 705−714.

(4) Furukawa, H.; Cordova, K. E.; O'Keeffe, M.; Yaghi, O. M. The Chemistry and Applications of Metal Organic Frameworks. *Science* **2013**, *341*, No. 1230444.

(5) Medishetty, R.; Zaręba, J. K.; Mayer, D.; Samoć, M.; Fischer, R. A. Nonlinear Optical Properties, Upconversion and Lasing in Metal−Organic Frameworks. *Chem. Soc. Rev.* **2017**, *46*, 4976−5004.

(6) Wang, H.; Vagin, S. I.; Lane, S.; Lin, W.; Shyta, V.; Heinz, W. R.; Van Dyck, C.; Bergren, A. J.; Gardner, K.; Rieger, B.; Meldrum, A. Metal−Organic Framework with Color Switching and Strongly Polarized Emission. *Chem. Mater.* **2019**, *31*, 5816−5823.

(7) Dhakshinamoorthy, A.; Li, Z.; Garcia, H. Catalysis and Photocatalysis by Metal Organic Frameworks. *Chem. Soc. Rev.* **2018**, *47*, 8134−8172.

(8) Jiao, L.; Wang, Y.; Jiang, H. L.; Xu, Q. Metal−Organic Frameworks as Platforms for Catalytic Applications. *Adv. Mater.* **2018**, *30*, No. 1703663.

(9) Valvekens, P.; Vermoortele, F.; De Vos, D. Metal Organic Frameworks as Catalysts: The Role of Metal Active Sites. *Catal. Sci. Technol.* **2013**, *3*, 1435−1445.

(10) Vermoortele, F.; Ameloot, R.; Alaerts, L.; Matthessen, R.; Carlier, B.; Fernandez, E. V. R.; Gascon, J.; Kapteijn, F.; De Vos, D. E. Tuning the Catalytic Performance of Metal Organic Frameworks in Fine Chemistry by Active Site Engineering. *J. Mater. Chem.* **2012**, *22*, 10313−10321.

(11) Wang, Y.; Wöll, C. Chemical Reactions at Isolated Single Sites Inside Metal−Organic Frameworks. *Catal. Lett.* **2018**, *148*, 2201−2222.

(12) Tilley, R. J. D. Defects in Solids. *Encyclopedia of Inorganic Chemistry*; John Wiley & Sons, Ltd., 2006.

(13) Vermoortele, F.; Bueken, B.; Le Bars, G.; Van de Voorde, B.; Vandichel, M.; Houthoofd, K.; Vimont, A.; Daturi, M.; Waroquier, M.; Van Speybroeck, V.; Kirschhock, C.; De Vos, D. E. Synthesis Modulation as a Tool To Increase the Catalytic Activity of Metal−Organic Frameworks: The Unique Case of UiO 66(Zr). *J. Am. Chem. Soc.* **2013**, *135*, 11465−11468.

(14) Tu, B.; Pang, Q.; Wu, D.; Song, Y.; Weng, L.; Li, Q. Ordered Vacancies and Their Chemistry in Metal−Organic Frameworks. *J. Am. Chem. Soc.* **2014**, *136*, 14465−14471.

(15) Canivet, J.; Vandichel, M.; Farrusseng, D. Origin of Highly Active Metal Organic Framework Catalysts: Defects? Defects! *Dalton Trans.* **2016**, *45*, 4090−4099.

(16) Cheetham, A. K.; Bennett, T. D.; Coudert, F. X.; Goodwin, A. L. Defects and Disorder in Metal Organic Frameworks. *Dalton Trans.* **2016**, *45*, 4113−4126.

(17) Shearer, G. C.; Chavan, S.; Bordiga, S.; Svelle, S.; Olsbye, U.; Lillerud, K. P. Defect Engineering: Tuning the Porosity and Composition of the Metal−Organic Framework UiO 66 via Modulated Synthesis. *Chem. Mater.* **2016**, *28*, 3749−3761.

(18) Dissegna, S.; Epp, K.; Heinz, W. R.; Kieslich, G.; Fischer, R. A. Defective Metal Organic Frameworks. *Adv. Mater.* **2018**, *30*, No. 1704501.

(19) Fang, Z.; Bueken, B.; De Vos, D. E.; Fischer, R. A. Defect Engineered Metal−Organic Frameworks. *Angew. Chem., Int. Ed.* **2015**, *54*, 7234−7254.

(20) Taddei, M. When Defects Turn into Virtues: The Curious Case of Zirconium Based Metal Organic Frameworks. *Coord. Chem. Rev.* **2017**, *343*, 1−24.

(21) Noei, H.; Kozachuk, O.; Amirjalayer, S.; Bureekaew, S.; Kauer, M.; Schmid, R.; Marler, B.; Muhler, M.; Fischer, R. A.; Wang, Y. CO Adsorption on a Mixed Valence Ruthenium Metal−Organic Frame work Studied by UHV FTIR Spectroscopy and DFT Calculations. *J. Phys. Chem. C* **2013**, *117*, 5658−5666.

(22) Kozachuk, O.; Luz, I.; Llabrés i Xamena, F. X.; Noei, H.; Kauer, M.; Albada, H. B.; Bloch, E. D.; Marler, B.; Wang, Y.; Muhler, M.; Fischer, R. A. Multifunctional, Defect Engineered Metal−Organic Frameworks with Ruthenium Centers: Sorption and Catalytic Properties. *Angew. Chem., Int. Ed.* **2014**, *53*, 7058−7062.

(23) Zhang, W.; Kauer, M.; Halbherr, O.; Epp, K.; Guo, P.; Gonzalez, M. I.; Xiao, D. J.; Wiktor, C.; Xamena, F. X. L. i.; Wöll, C.; Wang, Y.; Muhler, M.; Fischer, R. A. Ruthenium Metal−Organic Frameworks with Different Defect Types: Influence on Porosity, Sorption, and Catalytic Properties. *Chem. Eur. J.* **2016**, *22*, 14297−14307.

(24) Fang, Z.; Dürholt, J. P.; Kauer, M.; Zhang, W.; Lochenie, C.; Jee, B.; Albada, B.; Metzler Nolte, N.; Pöppl, A.; Weber, B.; Muhler, M.; Wang, Y.; Schmid, R.; Fischer, R. A. Structural Complexity in Metal−Organic Frameworks: Simultaneous Modification of Open Metal Sites and Hierarchical Porosity by Systematic Doping with Defective Linkers. *J. Am. Chem. Soc.* **2014**, *136*, 9627−9636.

(25) Taddei, M.; Wakeham, R. J.; Koutsianos, A.; Andreoli, E.; Barron, A. R. Post Synthetic Ligand Exchange in Zirconium Based Metal−Organic Frameworks: Beware of The Defects! *Angew. Chem., Int. Ed.* **2018**, *57*, 11706−11710.

(26) Chun, H.; Bak, W.; Hong, K.; Moon, D. A Simple and Rational Approach for Binodal Metal−Organic Frameworks with Tetrahedral Nodes and Unexpected Multimodal Porosities from Nonstoichio metric Defects. *Cryst. Growth Des.* **2014**, *14*, 1998−2002.

(27) St. Petkov, P.; Vayssilov, G. N.; Liu, J.; Shekhah, O.; Wang, Y.; Wöll, C.; Heine, T. Defects in MOFs: A Thorough Characterization. *ChemPhysChem* **2012**, *13*, 2025−2029.

(28) Wang, Z.; Sezen, H.; Liu, J.; Yang, C.; Roggenbuck, S. E.; Peikert, K.; Fröba, M.; Mavrandonakis, A.; Supronowicz, B.; Heine, T.; Gliemann, H.; Wöll, C. Tunable Coordinative Defects in UHM 3 Surface Mounted MOFs for Gas Adsorption and Separation: A Combined Experimental and Theoretical Study. *Microporous Meso porous Mater.* **2015**, *207*, 53−60.

(29) Bentley, J.; Foo, G. S.; Rungta, M.; Sangar, N.; Sievers, C.; Sholl, D. S.; Nair, S. Effects of Open Metal Site Availability on Adsorption Capacity and Olefin/Paraffin Selectivity in the Metal−Organic Framework Cu3(BTC)2. *Ind. Eng. Chem. Res.* **2016**, *55*, 5043−5053.

(30) Dang, S.; Zhu, Q. L.; Xu, Q. Nanomaterials Derived from Metal−Organic Frameworks. *Nat. Rev. Mater.* **2018**, *3*, No. 17075.

(31) Hussain, M. Z.; Schneemann, A.; Fischer, R. A.; Zhu, Y.; Xia, Y. MOF Derived Porous ZnO/C Nanocomposites for Efficient Dye Photodegradation. *ACS Appl. Energy Mater.* **2018**, *1*, 4695−4707.

(32) Yang, Y.; Dong, H.; Wang, Y.; He, C.; Wang, Y.; Zhang, X. Synthesis of Octahedral Like Cu BTC Derivatives Derived from MOF Calcined under Different Atmosphere for Application in CO Oxidation. *J. Solid State Chem.* **2018**, *258*, 582−587.

(33) Chui, S. Y.C.; Lo, S. M. F.; Charmant, J. P. H.; Orpen, A. G.; Williams, I. D. A Chemically Functionalizable Nanoporous Material [Cu3(TMA)2(H2O)3]n. *Science* **1999**, *283*, 1148−1150.

(34) Kozachuk, O.; Yusenko, K.; Noei, H.; Wang, Y.; Walleck, S.; Glaser, T.; Fischer, R. A. Solvothermal Growth of a Ruthenium Metal−Organic Framework Featuring HKUST 1 Structure Type as Thin Films on Oxide Surfaces. *Chem. Commun.* **2011**, *47*, 8509−8511.

(35) Zhang, W.; Freitag, K.; Wannapaiboon, S.; Schneider, C.; Epp, K.; Kieslich, G.; Fischer, R. A. Elaboration of a Highly Porous RuII,II Analogue of HKUST 1. *Inorg. Chem.* **2016**, *55*, 12492−12495.

(36) Zhang, W.; Kozachuk, O.; Medishetty, R.; Schneemann, A.; Wagner, R.; Khaletskaya, K.; Epp, K.; Fischer, R. A. Controlled SBU Approaches to Isoreticular Metal Organic Framework Ruthenium Analogues of HKUST 1. *Eur. J. Inorg. Chem.* **2015**, *2015*, 3913−3920.

(37) Kumar, D. K.; Filatov, A. S.; Napier, M.; Sun, J.; Dikarev, E. V.; Petrukhina, M. A. Dirhodium Paddlewheel with Functionalized Carboxylate Bridges: New Building Block for Self Assembly and Immobilization on Solid Support. *Inorg. Chem.* **2012**, *51*, 4855−4861.

(38) Kitamura, H.; Ozawa, T.; Jitsukawa, K.; Masuda, H.; Aoyama, Y.; Einaga, H. Syntheses, Structures, and Properties of Tetrakis(mu acetato)dirhodium(II) Complexes with Axial Pyridine Nitrogen Donor Ligands with or without Assistance of Hydrogen Bonds. *Inorg. Chem.* **2000**, *39*, 3294−300.

(39) Nickerl, G.; Stoeck, U.; Burkhardt, U.; Senkovska, I.; Kaskel, S. A Catalytically Active Porous Coordination Polymer Based on a Dinuclear Rhodium Paddle Wheel Unit. *J. Mater. Chem. A* **2014**, *2*, 144−148.

(40) Heinz, W. R.; Kratky, T.; Drees, M.; Wimmer, A.; Tomanec, O.; Günther, S.; Schuster, M.; Fischer, R. A. Mixed Precious Group Metal−Organic Frameworks: A Case Study of the HKUST 1 Analogue [RuxRh3−x(BTC)2]. *Dalton Trans.* **2019**, *48*, 12031−12039.

(41) Zhang, W.; Chen, Z.; Al Naji, M.; Guo, P.; Cwik, S.; Halbherr, O.; Wang, Y.; Muhler, M.; Wilde, N.; Glaser, R.; Fischer, R. A. Simultaneous Introduction of Various Palladium Active Sites into MOF via One Pot Synthesis: Pd@[Cu3 xPdx(BTC)2]n. *Dalton Trans.* **2016**, *45*, 14883−14887.

(42) Guo, P.; Froese, C.; Fu, Q.; Chen, Y. T.; Peng, B.; Kleist, W.; Fischer, R. A.; Muhler, M.; Wang, Y. CuPd Mixed Metal HKUST 1 as a Catalyst for Aerobic Alcohol Oxidation. *J. Phys. Chem. C* **2018**, *122*, 21433−21440.

(43) Shakya, D. M.; Ejegbavwo, O. A.; Rajeshkumar, T.; Senanayake, S. D.; Brandt, A. J.; Farzandh, S.; Acharya, N.; Ebrahim, A. M.; Frenkel, A. I.; Rui, N.; Tate, G. L.; Monnier, J. R.; Vogiatzis, K. D.; Shustova, N. B.; Chen, D. A. Selective Catalytic Chemistry at Rhodium(II) Nodes in Bimetallic Metal−Organic Frameworks. *Angew. Chem., Int. Ed.* **2019**, *58*, 16533−16537.

(44) Zhang, W.; Kozachuk, O.; Medishetty, R.; Schneemann, A.; Wagner, R.; Khaletskaya, K.; Epp, K.; Fischer, R. A. Controlled SBU Approaches to Isoreticular Metal Organic Framework Ruthenium Analogues of HKUST 1. *Eur. J. Inorg. Chem.* **2015**, *2015*, 3913−3920.

(45) Picheau, E.; Hof, F.; Derré, A.; Daffos, B.; Pénicaud, A. Thermal Oxidation of Carbonaceous Nanomaterials Revisited: Evidence of Mechanism Changes. *Angew. Chem., Int. Ed.* **2019**, *58*, 16013−16017.

(46) Epp, K.; Luz, I.; Heinz, W. R.; Rapeyko, A.; Llabres i Xamena, F. X.; Fischer, R. A. Defect Engineered Ruthenium MOFs as Versatile Hydrogenation Catalysts. *ChemCatChem* **2020**, *12*, 1720−1725.

(47) Aguirrezabal Telleria, I.; Luz, I.; Ortuño, M. A.; Oregui Bengoechea, M.; Gandarias, I.; López, N.; Lail, M. A.; Soukri, M. Gas Reactions Under Intrapore Condensation Regime within Tailored Metal−Organic Framework Catalysts. *Nat. Commun.* **2019**, *10*, No. 2076.

(48) Lee, S. J.; Doussot, C.; Baux, A.; Liu, L.; Jameson, G. B.; Richardson, C.; Pak, J. J.; Trousselet, F.; Coudert, F. X.; Telfer, S. G. Multicomponent Metal−Organic Frameworks as Defect Tolerant Materials. *Chem. Mater.* **2016**, *28*, 368−375.

(49) De Jesus, J. C.; González, I.; Quevedo, A.; Puerta, T. Thermal Decomposition of Nickel Acetate Tetrahydrate: An Integrated Study by TGA, QMS and XPS Techniques. *J. Mol. Catal. A: Chem.* **2005**, *228*, 283−291.

(50) Hayes, J. C.; Guan, H.; Collias, D. I. Production of Terephthalic Acid via Reductive Coupling of Propiolic Acid or Propiolic Acid Derivatives. U.S. Patent WO2016149091(A, 2016.

(51) Friedman, S.; Kaufman, M. L.; Wender, I. The Metal Carbonyl Catalyzed Decarboxylation of Aromatic Anhydrides and Acids. *Ann. N.Y. Acad. Sci.* **1967**, *145*, 141−149.

(52) Shearer, G. C.; Chavan, S.; Ethiraj, J.; Vitillo, J. G.; Svelle, S.; Olsbye, U.; Lamberti, C.; Bordiga, S.; Lillerud, K. P. Tuned to

Perfection: Ironing Out the Defects in Metal−Organic Framework UiO 66. *Chem. Mater.* **2014**, *26*, 4068−4071.

(53) Howarth, A. J.; Liu, Y.; Li, P.; Li, Z.; Wang, T. C.; Hupp, J. T.; Farha, O. K. Chemical, Thermal and Mechanical Stabilities of Metal−Organic Frameworks. *Nat. Rev. Mater.* **2016**, *1*, No. 15018.

(54) Farrusseng, D.; Daniel, C.; Gaudillère, C.; Ravon, U.; Schuurman, Y.; Mirodatos, C.; Dubbeldam, D.; Frost, H.; Snurr, R. Q. Heats of Adsorption for Seven Gases in Three Metal−Organic Frameworks: Systematic Comparison of Experiment and Simulation. *Langmuir* **2009**, *25*, 7383−7388.

(55) Kanoo, P.; Reddy, S. K.; Kumari, G.; Haldar, R.; Narayana, C.; Balasubramanian, S.; Maji, T. K. Unusual Room Temperature CO2 Uptake in a Fluoro Functionalized MOF: Insight from Raman Spectroscopy and Theoretical Studies. *Chem. Commun.* **2012**, *48*, 8487−8489.

(56) Gao, Q.; Xu, J.; Cao, D.; Chang, Z.; Bu, X. H. A Rigid Nested Metal−Organic Framework Featuring a Thermoresponsive Gating Effect Dominated by Counterions. *Angew. Chem., Int. Ed.* **2016**, *55*, 15027−15030.

(57) Cai, G.; Jiang, H. L. A Modulator Induced Defect Formation Strategy to Hierarchically Porous Metal−Organic Frameworks with High Stability. *Angew. Chem., Int. Ed.* **2017**, *56*, 563−567.

(58) Hu, Z.; Peng, Y.; Gao, Y.; Qian, Y.; Ying, S.; Yuan, D.; Horike, S.; Ogiwara, N.; Babarao, R.; Wang, Y.; Yan, N.; Zhao, D. Direct Synthesis of Hierarchically Porous Metal−Organic Frameworks with High Stability and Strong Brønsted Acidity: The Decisive Role of Hafnium in Efficient and Selective Fructose Dehydration. *Chem. Mater.* **2016**, *28*, 2659−2667.

(59) Aquino, M. A. S. Diruthenium and Diosmium Tetracarbox ylates: Synthesis, Physical Properties and Applications. *Coord. Chem. Rev.* **1998**, *170*, 141−202.

(60) Rusjan, M.; Sileo, E. E.; Cukiernik, F. D. Thermal Stability of Mixed Valent Diruthenium (II,III) Carboxylates. *Solid State Ion.* **2003**, *159*, 389−396.

(61) Rusjan, M. C.; Sileo, E. E.; Cukiernik, F. D. Thermal Decomposition of Mixed Valent Diruthenium Pentakis(alkanoates) Enhanced by Their Liquid Crystalline State. *Solid State Ion.* **1999**, *124*, 143−147.

(62) Delen, G.; Ristanović, Z.; Mandemaker, L. D. B.; Weckhuysen, B. M. Mechanistic Insights into Growth of Surface Mounted Metal Organic Framework Films Resolved by Infrared (Nano) Spectros copy. *Chem. Eur. J.* **2018**, *24*, 187−195.

(63) Mahalakshmi, G.; Balachandran, V. FT IR and FT Raman Spectra, Normal Coordinate Analysis and Ab Initio Computations of Trimesic Acid. *Spectrochim. Acta, Part A* **2014**, *124*, 535−547.

(64) Prestipino, C.; Regli, L.; Vitillo, J. G.; Bonino, F.; Damin, A.; Lamberti, C.; Zecchina, A.; Solari, P. L.; Kongshaug, K. O.; Bordiga, S. Local Structure of Framework Cu(II) in HKUST 1 Metallorganic Framework: Spectroscopic Characterization upon Activation and Interaction with Adsorbates. *Chem. Mater.* **2006**, *18*, 1337−1346.

(65) Palacios, E. G.; Juárez López, G.; Monhemius, A. J. Infrared Sectroscopy of Metal Carboxylates: II. Analysis of Fe(III), Ni and Zn Carboxylate Solutions. *Hydrometallurgy* **2004**, *72*, 139−148.

(66) Socrates, G. *Infrared and Raman Characteristic Group Frequencies: Tables and Charts*; Wiley, 2004.

(67) Zhang, W.; Kauer, M.; Halbherr, O.; Epp, K.; Guo, P.; Gonzalez, M. I.; Xiao, D. J.; Wiktor, C.; Liabrés i Xamena, F. X.; Wöll, C.; Wang, Y.; Muhler, M.; Fischer, R. A. Ruthenium Metal−Organic Frameworks with Different Defect Types: Influence on Porosity, Sorption, and Catalytic Properties. *Chem. Eur. J.* **2016**, *22*, 14297−14307.

(68) Wöll, C. Structure and Chemical Properties of Oxide Nanoparticles Determined by Surface Ligand IR Spectroscopy. *ACS Catal.* **2020**, *10*, 168−176.

(69) Wang, W.; Sharapa, D. I.; Chandresh, A.; Nefedov, A.; Heißler, S.; Heinke, L.; Studt, F.; Wang, Y.; Wöll, C. Interplay of Electronic and Steric Effects to Yield Low Temperature CO Oxidation at Metal Single Sites in Defect Engineered HKUST 1. *Angew. Chem., Int. Ed.* **2020**, *59*, 10514−10518.

Repository KITopen